

**₁ Ionospheric Electron Number Densities from
₂ CUTLASS dual-frequency Velocity Measurements
₃ using artificial backscatter over EISCAT**

Lois K. Sarno-Smith^{1,2}, Michael Kosch^{2,3,4}, Timothy Yeoman³, Michael

Rietveld^{5,6}, Amore' Nel^{2,7}, Michael W. Liemohn¹

Corresponding author: Lois K. Sarno-Smith, Department of Climate and Space, University of Michigan, Ann Arbor, Michigan, USA. (loisks@umich.edu)

¹Department of Climate and Space

4 **Abstract.**

5 Using quasi-simultaneous line of sight velocity measurements at multiple
6 frequencies from the Hankasalmi Cooperative UK Twin Auroral Sounding
7 System (CUTLASS) on the Super Dual Auroral Radar Network (SuperDARN),
8 we calculate electron number densities using a derivation outlined in *Gillies*
9 *et al.* [2010, 2012]. Backscatter targets were generated using the European
10 Incoherent Scatter (EISCAT) ionospheric modification facility at Tromsø,
11 Norway. We use two methods on two case studies. The first approach is to
12 use the dual frequency capability on CUTLASS and compare line of sight

Sciences and Engineering, University of
Michigan, Ann Arbor, Michigan, USA.

²South African National Space Agency,
Hermanus, RSA.

³University of Lancaster, Lancaster, UK.

⁴University of Western Cape, Cape Town,
RSA

⁵EISCAT Scientific Association

⁶University of Tromsø, The Arctic
University of Norway, Tromsø, Norway

⁷North-West University, Potchefstroom,
RSA

13 velocities between frequencies with a MHz or greater difference. The other
14 method used the kHz frequency shifts automatically made by the SuperDARN
15 radar during routine operations. Using ray tracing to obtain the approximate
16 altitude of the backscatter, we demonstrate that for both methods, Super-
17 DARN significantly overestimates N_e compared to those obtained from the
18 EISCAT incoherent scatter radar over the same time period. The discrep-
19 ancy between the N_e measurements of both radars may be largely due to Su-
20 perDARN sensitivity to backscatter produced by localized density irregu-
21 larities which obscure the background levels.

1. Introduction

22 The Super Dual Auroral Radar Network (SuperDARN) consists of thirty five coher-
23 ent scatter high frequency (HF) radars stationed throughout the world [*Greenwald et al.*,
24 1995; *Chisham et al.*, 2007; *Baker et al.*, 2011]. SuperDARN radars record the Doppler
25 velocity of ionospheric plasma irregularities and can provide large area convection maps
26 of the F region [*Ponomarenko et al.*, 2008; *Thomas et al.*, 2013]. However, velocity mea-
27 surements from SuperDARN are determined with assumption that the index of refraction
28 of the scattering volume is 1.0. In reality, the index of refraction is typically closer to
29 0.8 [*Gillies et al.*, 2009]. This overestimation of the refractive index leads to a consistent
30 underestimation of the Doppler velocity [*Eglitis et al.*, 1998; *Davies et al.*, 1999; *Xu et al.*,
31 2001].

32
33 The estimation of index of refraction can be corrected using ionospheric electron number
34 densities (N_e) from models such as the International Reference Ionosphere (IRI) or local
35 ionosonde measurements [*Bilitza*, 2001]. Since the scattering area of each SuperDARN
36 radar is so large (approximately 4×10^6 km²), direct comparison can lead to ambiguities
37 due to localized blobs and convection [*Norman et al.*, 2004; *de Larquier et al.*, 2011]. A
38 reliable method to calculate the actual index of refraction from SuperDARN observations
39 will lead to better Doppler velocity measurements from backscatter when plasma irregu-
40 larities are present.

41

42 *Gillies et al.* [2010, 2012] demonstrated theoretically that the index of refraction can
43 be calculated from dual frequency observations using SuperDARN. We can subsequently
44 calculate N_e from the plasma frequency. This method is valid as long as the SuperDARN
45 radar shifts the operating frequency of the radar on a time scale where the ionosphere is
46 stationary and if the difference of ray propagation paths at the two frequencies is small.
47 *Gillies et al.* [2012] showed statistical results of the derived SuperDARN electron number
48 densities from all the available SuperDARN radars from 1993-2012. However, no direct
49 comparison of plasma density between SuperDARN and another independent method was
50 presented. They also compared the observed line of sight velocities to those measured by
51 the Defense Meteorological Satellite Program (DMSP) and the European Incoherent Scatter
52 (EISCAT) radar. The velocities matched extremely well when the index of refraction
53 was accounted for (0.99 best fit line slope) [*Gillies et al.*, 2012].

54
55 Links between ionospheric density irregularities, gravity waves, particle precipitation,
56 and satellite drag prompted the need for large coverage and accurate electron number den-
57 sity measurements [*Drell et al.*, 1965; *Hooke*, 1968; *Robinson et al.*, 1987]. Previous work
58 has calculated electron number densities from SuperDARN measurements using ground
59 scatter [*André et al.*, 1998]. If SuperDARN can provide reliable N_e measurements, the
60 scientific community will have access to near global N_e coverage at high latitudes. This
61 would, for example, permit quasi-real time global studies of Joule heating in the E-region
62 [*Kosch and Nielsen*, 1995] or F-region [*Cierpka et al.*, 2000].

63

64 We expand the *Gillies et al.* [2012] study to directly compare the SuperDARN calcu-
65 lated N_e to EISCAT incoherent scatter electron number densities. By generating artificial
66 plasma irregularities (striations) with the EISCAT Heater [*Rietveld et al.*, 1993] at Tromsø
67 to create an artificial ‘target’ for SuperDARN backscatter, we can then use ray tracing to
68 localize the backscatter and directly compare the SuperDARN radar N_e with the EISCAT
69 N_e [*Kosch et al.*, 2004; *Wright et al.*, 2006; *Yeoman et al.*, 2008]. The EISCAT N_e are
70 derived from incoherent backscatter power accounting for the electron to ion tempera-
71 ture ratio in a fitting procedure using the Grand Unified Incoherent Scatter Design and
72 Analysis Package (GUISDAP) software [*Lehtinen and Huuskonen*, 1996]. Our analysis is
73 the first real test on the accuracy of the SuperDARN-based electron density estimates.
74 The analysis tests credibility of the method for global-scale electron density monitoring
75 for the case of multiple-radar utilization. We use the Co-operative UK Twin Located
76 Auroral Sounding System (CUTLASS) Hankasalmi SuperDARN radar (62.32 N, 26.61 E,
77 geographic coordinates) [*Lester et al.*, 2004] for comparison with EISCAT (69.6 N, 19.2
78 E, geographic coordinates) [*Rishbeth and Van Eyken*, 1993]. CUTLASS offers the unique
79 advantage of simultaneous transmission and reception of two independent signals. This
80 STEREO capability is powerful since it allows the SuperDARN radar to essentially act
81 as two independent radars. Thus, we can calculate electron densities using simultaneous
82 measurements with 1 MHz or more frequency separation (e.g. 15 and 16 MHz). Differ-
83 ent frequency rays will propagate to different altitudes along their paths in the F-region.
84 However, it has been shown that pump-induced artificial striations extend 10s of km in al-
85 titude [*Senior et al.*, 2004]. So, we can reasonably expect backscatter from similar ranges

at different frequencies to come from about the same irregularity regions.

The results of our study demonstrate that N_e calculated from Hankasalmi radar measurements are sensitive to the frequencies used to derive the N_e and overestimate N_e compared to EISCAT values. We use two controlled Heater experiments, one at daytime and one in the afternoon/evening, to provide artificial backscatter targets and narrow spectral widths in the Hankasalmi line of sight velocities. We also show that the method using smaller frequency shifts on the kHz scale also overestimates N_e compared to EISCAT.

2. Methodology

The index of refraction, n_s , can be calculated using the plasma frequency f_p and the radar wave frequency f :

$$n_s = \sqrt{1 - f_p^2/f^2} \quad (1)$$

and *Gillies et al.* [2011] showed that f_p could be calculated using two radar frequency observations of line of sight velocity, v :

$$f_p^2 = \frac{f_1^2(1 - v_1^2/v_2^2)}{1 - v_1^2 f_1^2/v_2^2 f_2^2} \quad (2)$$

102 Only observations where $v_1/v_2 < 1$ are physically meaningful for calculating index of re-
 103 fraction in this study. From this, we can calculate N_e (m^{-3}) from the f_p (Hz) as:

104

$$N_e = \frac{m_e \epsilon_0}{q^2} (2\pi f_p)^2 \quad (3)$$

105 where m_e is the mass of an electron, ϵ_0 is the permittivity of free space, and q is the charge
 106 of an electron. SuperDARN mono-frequency radars, by stepping the frequency every few
 107 seconds, can be used to calculate N_e from f_1 and f_2 . With the dual frequency STEREO
 108 capability, available on Hankasalmi, we operate the radar at two major frequency bands
 109 (e.g. 15 and 16 MHz) with incremental steps (kHz) in each band every few seconds.

110

111 We use data from two experiments. The first experiment was conducted on March 12,
 112 2015 10:00 to 12:01 UT, or 11:00 to 13:01 LT in Tromsø. During this daytime interval, Kp
 113 was at 2+. The CUTLASS Hankasalmi radar (62.3°N, 26.6°E) was operated at 15 and 16
 114 MHz sequentially between 10:00 - 11:21 UT. From 11:22 UT to 12:01 UT, the frequency
 115 was shifted between three major frequency bands at 16 MHz, 17 MHz, and 18 MHz. For
 116 the first case study, the 15 MHz band contained frequencies between 15.0 to 15.1 MHz, the
 117 16 MHz band contained frequencies from 16.2 to 16.7 MHz, the 17 MHz band contained
 118 frequencies from 17.9 MHz to 18.1 MHz, and the 18 MHz band contained frequencies from
 119 18.8 to 18.9 MHz. The radar operated on beam 5 with range gates beginning at 480 km
 120 and spaced 15 km apart with 1 second integration on each frequency sequentially, i.e. the
 121 cycle was either 2 seconds or 3 seconds long.

122

123 The EISCAT Heater operated with its beam field-aligned to the local magnetic field (at
124 a height of 240 km) at 6.2 MHz between 10:00 - 11:21 UT and then changed to 6.96 MHz
125 between 11:21 - 12:01 UT. The radiation from the Heater was in ordinary polarization
126 mode. Ionospheric pumping was slightly under dense, where the radiation frequency is
127 greater than the peak plasma frequency, throughout the interval. However, many past
128 experiments have shown this can still produce striations [*Leyser et al.*, 1990; *Gurevich*
129 *et al.*, 1995]. The effective radiated power (ERP) was 53 MW between 10:00 - 11:21 UT
130 and 32 MW between 11:21 - 12:01 UT.

131

132 The second experiment was conducted on March 3, 2016 from 14:00 to 18:00 UT, or
133 15:00 to 19:00 LT in Tromsø, with $K_p < 2$ throughout the experiment. Part of the ex-
134 periment occurred after sunset (approximately 17:00 UT). The CUTLASS Hankasalmi
135 STEREO radar was operated alternating between 13 and 15 MHz on Channel A through-
136 out the entire interval and with, additionally, 16 MHz between 14:00 to 17:00 UT on
137 Channel B. For the second case study, the 13 MHz band contained frequencies between
138 13.2 to 13.3 MHz, the 15 MHz band contained frequencies between 15.0 to 15.1 MHz, and
139 the 16 MHz band contained frequencies between 16.2 to 16.7 MHz. The radar operated on
140 beam 5 with range gates beginning at 480 km and spaced 15 km apart on Channel A and
141 the range gates beginning at 180 km and incrementing 45 km on Channel B. Channel A
142 operating frequency was varied between 13 and 15 MHz, using 3 second integration with
143 a 6 second cycle time. Channel B measured only at 16 MHz using 3 second integration
144 and also a 3 second cycle time.

145

146 The EISCAT ionospheric modification facility operated with the beam pointing field-
147 aligned and between 4.04 MHz to 5.423 MHz with 5.423 MHz between 14:00 to 16:30 UT
148 with an ERP of 180 MW, 4.9128 MHz between 16:30 to 16:38 UT with an ERP of 154
149 MW, 4.544 MHz from 16:38 to 17:38 UT with an ERP of 131 MW, and 4.04 MHz from
150 17:45 to 18:00 UT with an ERP of 110 MW. Ionospheric heating was mostly over-dense,
151 where the radiation frequency was lower than the peak ionospheric plasma frequency,
152 during this experiment with the reflection altitude at approximately 220 km. For both
153 experiments, the EISCAT UHF radar observed field-aligned using the 32 x 20 alternat-
154 ing “beata” code with 10 μ s sampling. This gives 3 km range resolution, 5 second time
155 integration and covers between 49 and 694 km in range. The EISCAT N_e during both
156 experiments was calibrated with local ionosonde measurements.

157

158 Figure 1A shows the Hankasalmi radar line of sight velocities used in our N_e calculation
159 between range gates 25 and 38 for the March 12, 2015 experiment. Figure 1 assimilates
160 velocity measurements from 15-18 MHz frequencies. Figure 1B shows the spectral widths
161 over the same period. For most of the experiment the velocities are negative and the spec-
162 tral widths are small (< 50 m/s) which is characteristic of backscatter from artificially
163 generated striations.

164

165 Figure 2 further demonstrates that the velocity distribution for each frequency is largely
166 contained between 0 to -50 m/s. Figure 2A shows the velocities for 15 MHz, Figure 2B
167 shows 16 MHz velocities, Figure 2C is 17 MHz velocities, and Figure 2D is 18 MHz veloc-
168 ities. The bin widths in the bar plots are 50 m/s. In particular for the 17 MHz frequency,

169 the velocity distribution is strongly peaked at approximately -50 m/s. The small velocity
170 distribution is consistent with the narrow spectral width and is a feature of backscatter
171 from artificially generated striations.

172

173 A ray trace to determine the altitude CUTLASS observes over EISCAT is imperative for
174 our comparison. For the most accurate ray trace, a reliable angle of arrival measurement
175 is necessary. However, the angle of arrival information for Hankasalmi was unavailable
176 during both of our experiments. Figure 3A shows the ray trace between 5 and 40 degrees
177 elevation angles for the 16 MHz frequency channel on beam 5 for March 12, 2015. The
178 silver lines indicate every 4th range gate starting at 480 km (range gate 0). The black star
179 represents the approximate EISCAT radar location. The horizontal black lines represent
180 a ray for every 2 degrees of elevation angle. Based on where the last ray paths that refract
181 back to Earth are over Tromsø, we estimate that Hankasalmi observes between 200-260
182 km, which is consistent with the hmF2 peak from the ionosonde measurements on this day
183 at 240 km. For the following figures, we estimate that Hankasalmi observes backscatter
184 from 240 km on this day. When the same elevation angles are compared, higher frequen-
185 cies probe higher levels of the ionosphere, with a 1 MHz frequency difference producing
186 height differences from 5 km to 50 km. Similar results are obtained for March 3, 2016
187 (not shown). Here the Heater pump frequency corresponded to the ionospheric plasma
188 frequency at an altitude of approximately 220 km. In Figure 3B, we show the IRI and
189 EISCAT N_e profiles averaged between 9:30 to 12:00 UT on March 12, 2015 to demonstrate
190 that IRI and EISCAT provide similar N_e values below 300 km. Since the model values
191 from IRI are close to EISCAT, we can trust the ray trace in Figure 3A which relies on

192 IRI to calculate the index of refraction.

193

3. Results

194 We test two methods to determine if N_e can be reliably calculated from SuperDARN
195 radar data. We make use of the unique STEREO feature of the CUTLASS radar at
196 Hankasalmi, when it is available, which was in our experiment on March 3, 2016. At each
197 measurement, we first average the range gates of backscatter where Hankasalmi observes
198 irregularities produced by the EISCAT Heater, here defined as range gates 30-35. Then,
199 we resample the data to a 2 minute cadence in each frequency band. Simultaneous com-
200 parison and un-averaged measurements from several range gates results in noisy data,
201 which is why we spatially and temporally smooth the data before calculating the velocity
202 ratio between the two frequencies. If $v_1 > v_2$, the N_e values are unphysical because the
203 derivation of Equation 2 from Equation 1 assumes that, because the refractive index is
204 dependent on radar frequency, the velocity measured at the lower frequency (v_1) must be
205 lower than the velocity measured at the higher frequency (v_2). Therefore, we remove all
206 data when $v_1 > v_2$. There are 4 bands we compare from the first case study on March 12,
207 2015: 15-16 MHz, 16-17 MHz, 17-18 MHz, and 16-18 MHz and 3 bands from the second
208 case study on March 3, 2016 at 13-15 MHz, 13-16 MHz, and 15-16 MHz.

209

210 Table 1 shows the number of points used in the study before resampling the velocities
211 and the number of velocity points in the two minute resample. For the case study on
212 March 12, 2015, most of the velocity data is measured at 15 MHz (1024 points) or 16
213 MHz (1365 points) which are then down sampled to 23 points of conjunction between

214 the 15-16 MHz frequencies. For the case study on March 3, 2016, there are many points
215 spread between 13 MHz (1089 points), 15 MHz (1562 points), and 16 MHz (1710) while
216 Hankasalmi operated in dual frequency mode. This led to 39 2-minute interval conjunc-
217 tions between 13 and 15 MHz, 22 conjunction points between 13 and 16 MHz, and 32
218 conjunction points between 15 and 16 MHz. The number of down-sampled points in our
219 study is much lower than the 10^6 points used in *Gillies et al.* [2010].

220

221 The second method is to use the small frequency shifts of kHz that SuperDARN au-
222 tomatically makes as it scans within a selected frequency range. For instance, in the 15
223 MHz band we observe an approximate 1 kHz change every 2 seconds. The radar does this
224 to select the quietest frequency of observation, giving the highest signal-to-noise ratio.
225 Our second method uses this frequency shift by averaging the measurements in range
226 gates 30-35 at a given time and then calculating N_e from the average line of sight velocity
227 measurement and slightly shifted frequency two seconds later. We also remove times when
228 $v_1 > v_2$. This method requires assuming ionospheric stability over a 2 second interval but
229 with far smaller frequency shifts. We then resample these data to a 2 minute cadence to
230 reduce the noise of the measurements. The potential advantage of this method is that the
231 dual frequency STEREO mode of CUTLASS is not necessary and this method could be
232 implemented on all SuperDARN radars.

233

234 Figure 4 illustrates the differences in the two approaches for calculating N_e for both
235 case studies. Figure 4A shows the Hankasalmi data from March 12, 2015. The colored
236 triangles represent the N_e from wide frequency spacing, where red is 15-16 MHz, green

237 is 16-17 MHz, yellow is 16-18 MHz, and blue is 17-18 MHz. The monochrome hexagons
 238 represent the N_e calculated from small frequency shifts (kHz), with black as the 15 MHz
 239 measurements, dark grey is the 16 MHz measurements, light grey is the 17 MHz N_e , and
 240 white is the 18 MHz N_e . Figure 4B shows the Hankasalmi data from March 3, 2016 where
 241 the red triangles represent 13-15 MHz, green is 13-16 MHz, and yellow is 15-16 MHz. The
 242 gray scale hexagons represent the small frequency shift calculated N_e , with black as the
 243 13 MHz measurements, dark grey is the 15 MHz measurements, and light grey is the 16
 244 MHz N_e .

245

246 The most notable feature of this figure is the near constant values the small frequency
 247 shift calculated N_e exhibits. For example in Figure 4A, at 15 MHz, the calculated N_e
 248 value barely fluctuates from $2.7 \times 10^{12} \text{ m}^{-3}$ while the N_e from 16 MHz hovers at $3.3 \times$
 249 10^{12} m^{-3} . The N_e calculated from wide frequency spacing, on the other hand, shows some
 250 variability and changes in time in a more reasonable manner. The lack of variation in the
 251 N_e from small frequency shifts shows that this method is strongly influenced by the value
 252 of f_1 in Equation 2, which is the measuring frequency of the line of sight velocities. Larger
 253 values of f_1 correspond to larger N_e , with 17 and 18 MHz frequency data being the highest
 254 and producing similar values. This is consistent in Figure 4B with 16 MHz producing the
 255 largest N_e . The small frequency shift method of estimating N_e produces unrealistically
 256 static N_e values subject to the radar frequency, which is not consistent with expectation.

257

258 Figure 5 shows N_e calculated from the wide-frequency spacing from Hankasalmi com-
 259 pared to EISCAT and IRI N_e values. The N_e from Hankasalmi is approximately an order

260 of magnitude larger than the EISCAT and IRI N_e . The IRI N_e values are calculated on
261 an hourly timescale during the experiments from the Community Coordinated Modeling
262 Center (CCMC). In Figure 5A, the colored triangles represent the N_e from Hankasalmi,
263 where red is the 15-16 MHz, green is the 16-17 MHz, yellow is the 16-18 MHz, and blue
264 is the 17-18 MHz observations on March 12, 2015. In Figure 5B, the colored triangles
265 represent the N_e from Hankasalmi, where red is the 13-15 MHz, green is the 13-16 MHz,
266 and yellow is the 15-16 MHz observations on March 3, 2016. In Figure 5A, the grey
267 diamonds are the 2-minute resampled N_e from EISCAT at 240 km and the dotted blue
268 line is the IRI data over this time range at 240 km. For Figure 5B, EISCAT and IRI N_e
269 are taken from 220 km.

270

271 The Hankasalmi derived N_e does not capture the $1 \times 10^{11} \text{ m}^{-3}$ increase that EISCAT
272 measures starting at 10:50 UT in Figure 5A. Instead, the Hankasalmi derived N_e remains
273 somewhat constant between 10:00 to 11:30 UT and then jumps up by $1 \times 10^{12} \text{ m}^{-3}$ when
274 different frequencies are employed. Like the small frequency shift results, this suggests
275 that the N_e derived from the dual frequency mode is sensitive to the value of f_1 used in
276 Equation 2 and this can affect the results significantly. The IRI and EISCAT N_e agree
277 very well throughout the time period, with IRI slightly higher than EISCAT.

278

279 In Figure 5B, the Hankasalmi derived N_e completely fails to capture the ionospheric
280 N_e decrease in the EISCAT data at 16:00 UT. The results from the March 3, 2016 case
281 study are also more variable than the March 12, 2015 case study in Figure 5A, ranging
282 from very close to EISCAT N_e values to being off by a factor of 20. Once again, the IRI

283 and EISCAT N_e values are very close, with IRI slightly lower than EISCAT in Figure 5B.
284 Overall, the data shown in Figure 5 demonstrate that deriving N_e from dual frequency
285 measurements is not a reliable method for calculating background N_e from SuperDARN
286 measurements.

287
288 We also use linear regression to quantify the correlation coefficient (r) between the 2
289 minute resampled N_e from EISCAT and Hankasalmi despite the order of magnitude dif-
290 ference between the data sets. For the first experiment, the r between 15-16 MHz was
291 0.09, for 16-17 MHz was -0.13, for 16-18 MHz was 0.03, and for 17-18 MHz was 0.17. For
292 the second experiment, the r between 13-15 MHz was -0.049, for 13-16 MHz was -0.015,
293 and between 15-16 MHz was -0.017. All of the linear regression correlation coefficients cal-
294 culated between the N_e from Hankasalmi and EISCAT are extremely low, demonstrating
295 that the N_e derived from Hankasalmi fails to capture the trends measured by EISCAT.
296 On the other hand, the linear regression r between EISCAT and IRI is 0.97 for the first
297 experiment and 0.99 for the second experiment.

298
299 The Hankasalmi N_e is approximately an order of magnitude larger than the EISCAT
300 N_e . Figure 6 shows the N_e from Hankasalmi divided by the EISCAT N_e at about 240 km,
301 both resampled to the same 2 minute cadence between 10:00 to 12:00 UT on March 12,
302 2015 and 14:00 to 18:00 on March 3, 2016 at approximately 220 km. The black dotted line
303 represents where the Hankasalmi data would match the EISCAT N_e . The colored trian-
304 gles represent the different frequency bands used to calculate N_e , as previously described.
305 In Figure 6A, the N_e derived from the 15-16 MHz observations shows the most variation

306 and difference from the EISCAT N_e early in the experiment from 10:00 to 10:30 UT. After
307 10:30 UT, the Hankasalmi N_e measurements, regardless of frequency, are greater than the
308 EISCAT N_e by a factor of 6-10. The least variable ratio is the 17-18 MHz band for N_e
309 measurements, clustered around a factor of 8 difference.

310

311 In Figure 6B, all bands (13-15 MHz, 13-16 MHz, and 15-16 MHz) show large variation
312 and are consistently off from the EISCAT N_e . The offset ratio increases throughout the
313 experiment, reaching a maximum of approximately a factor of 15 by 17:00 UT. This is
314 because the N_e calculated from Hankasalmi observations do not capture the decrease in
315 the ionosphere as the sun sets and the ionosphere cools.

316

317 With a near order of magnitude overestimate of N_e , the Hankasalmi measurements do
318 not align well with the EISCAT N_e . The N_e derived from Hankasalmi observations also
319 does not capture the gradual increase in N_e seen by EISCAT after 10:50 UT in the first
320 case study nor the steady decrease of N_e in the second case study as the sun sets.

321

4. Discussion

322 Theoretically, calculating electron densities from frequency shifts in the SuperDARN
323 line of sight Doppler velocity observations should account for the index of refraction and
324 provide reliable electron density calculations. However, our comparison to EISCAT N_e
325 observations demonstrates that Hankasalmi derived N_e overestimated by approximately a
326 factor 8, which is dependent on the radar frequencies used to calculate N_e . This demon-
327 strates that the dual frequency method is not effective for calculating reliable background

328 N_e from SuperDARN observations.

329

330 *Gillies et al.* [2010] proposed that an overestimation of N_e could be from localized regions
331 of SuperDARN backscatter. For example, dominant scatter could be from a small fraction
332 of the SuperDARN range cell in which conditions for scatter are best. Whereas EISCAT
333 captures the background N_e , CUTLASS is prone to picking up localized structures which
334 produce stronger irregularities and places with higher electron density [*Hosokawa et al.*,
335 2009]. Further, N_e enhancements of up to an order of magnitude due to polar cap patches
336 are likely to occur during the day time, which is when our experiment on March 12, 2015
337 took place [*Sojka et al.*, 1990; *Pryse et al.*, 2005]. Polar cap patches have also been shown
338 to extend in the afternoon and evening, which would overlap with the times of our March
339 3, 2016 case study [*Moen et al.*, 2007; *Zhang et al.*, 2013]. Within a polar cap patch, elec-
340 tron number density can vary by an order of magnitude [*Weber et al.*, 1986]. All of this
341 was mitigated in the experiments presented above by running the EISCAT Heater during
342 these two intervals. This produced plasma irregularities over EISCAT and therefore scat-
343 tering along the line of sight of the Hankasalmi radar, making the Hankasalmi-EISCAT
344 observations ideal for direct comparison.

345

346 The field aligned density striations themselves could also contribute to the SuperDARN
347 N_e overestimation. *Gurevich et al.* [1999] showed that bunches of field aligned density
348 striations due to self-focusing of the Heater pump beam in the ionosphere could lead
349 to 10% N_e enhancements. The 10m scale striations observed by SuperDARN are not
350 large, so the density enhancements would not manifest themselves in the EISCAT N_e

351 observations but could be selectively picked out by SuperDARN. Several studies have
352 also shown that these field aligned striations from the EISCAT heating facility produce
353 a strong backscatter response in Hankasalmi measurements [*Kelley et al.*, 1995; *Dhillon*,
354 2002; *Kosch et al.*, 2002; *Gurevich et al.*, 2002; *Rietveld et al.*, 2003]. If we could resolve
355 the size of irregularity bunches compared to the scattering volume measured by Super-
356 DARN, it may be possible to reconcile N_e calculated from SuperDARN observations of
357 line of sight velocity measurements at different frequencies with EISCAT N_e . As stated,
358 though, these striations produce only a 10% density effect, and the Hankasalmi derived
359 N_e were off by an order of magnitude.

360

5. Conclusions

361 Our experiments on March 12, 2015 and March 3, 2016 compared calculated N_e , derived
362 from the CUTLASS Hankasalmi radar line of sight velocity measurements, to the Tromsø
363 EISCAT UHF incoherent scatter radar derived N_e . Our ray tracing estimates showed that
364 Hankasalmi was approximately probing the ionosphere at 240 km over Tromsø on March
365 12, 2015 and at 220 km on March 3, 2016. We found that the derivation for calculating
366 electron number densities proposed by *Gillies et al.* [2010, 2012] was unsuccessful at deter-
367 mining reasonable background N_e from pump-induced artificial striations over EISCAT.
368 No plasma density at any altitude could provide agreement. We tested the method using
369 near simultaneous dual frequency observations (MHz difference) and by also using the
370 automatic frequency shifts (kHz difference) typical of SuperDARN radars when operating
371 on one frequency band. Both methods overestimated N_e by approximately a factor of 8,
372 and, in particular, the small frequency shift method resulted in static, frequency depen-

373 dent results. Neither method captured EISCAT observed N_e increases or decreases across
374 the experimental window.

375
376 We propose that the overestimation of N_e by SuperDARN may be due to localized
377 density irregularities dominating the backscatter measured by SuperDARN and resulting
378 in an artificially high N_e based off of these localized irregularities. However, other factors
379 could contribute to the discrepancy between SuperDARN and EISCAT N_e , such as the
380 limited number of data points in our case studies.

381
382 **Acknowledgments.** The Michigan co-authors would like to thank the University of
383 Michigan Rackham Graduate school and the NSF GRFP program. EISCAT is an in-
384 ternational association supported by research organizations in China (CRIRP), Finland
385 (CSA), Japan (NIPR and STEL), Norway (NFR), Sweden (VR), and the United Kingdom
386 (NERC). Thanks also to the CCMC website for use of the IRI model, which is available
387 at: <http://ccmc.gsfc.nasa.gov/>. The authors would also like to thank the SuperDARN
388 team, in particular Evan Thomas, Kevin Sterne, Xueling Shi, Jo Baker, and Muhammad
389 Ahunbay for their invaluable assistance in the ray tracing procedure.

390
391 We would also, in particular, like to thank the NSF GROW with US-AID program for
392 sponsoring this collaboration in conjunction with the NSF GRFP program and the South
393 African National Space Agency (SANSA).

References

- 395 André, D., G. J. Sofko, K. Baker, and J. MacDougall (1998), SuperDARN interferome-
396 try: Meteor echoes and electron densities from ground scatter, *Journal of Geophysical*
397 *Research: Space Physics*, *103*(A4), 7003–7015.
- 398 Baker, J. B., J. M. Ruohoniemi, A. J. Ribeiro, L. B. Clausen, R. A. Greenwald, N. A.
399 Frissell, and K. A. Sterne (2011), SuperDARN ionospheric space weather, *Aerospace*
400 *and Electronic Systems Magazine, IEEE*, *26*(10), 30–34.
- 401 Bilitza, D. (2001), International Reference Ionosphere 2000, *Radio Science*, *36*(2), 261–
402 275.
- 403 Chisham, G., M. Lester, S. E. Milan, M. Freeman, W. Bristow, A. Grocott,
404 K. McWilliams, J. Ruohoniemi, T. K. Yeoman, P. L. Dyson, et al. (2007), A decade
405 of the Super Dual Auroral Radar Network (SuperDARN): Scientific achievements, new
406 techniques and future directions, *Surveys in Geophysics*, *28*(1), 33–109.
- 407 Cierpka, K., M. J. Kosch, M. Rietveld, K. Schlegel, T. Hagfors. (2000), Ion-neutral coupling
408 in the high-latitude F-layer from incoherent scatter and Fabry Perot interferometer
409 measurements, *Annales Geophysicae*, *18*(9), 1145–1153.
- 410 Davies, J., M. Lester, S. E. Milan, and T. Yeoman (1999), A comparison of velocity
411 measurements from the CUTLASS Finland radar and the EISCAT UHF system, in
412 *Annales Geophysicae*, vol. 17, pp. 892–902, Springer.
- 413 de Larquier, S., J. Ruohoniemi, J. Baker, N. Ravindran Varrier, and M. Lester (2011),
414 First observations of the midlatitude evening anomaly using Super Dual Auroral
415 Radar Network (SuperDARN) radars, *Journal of Geophysical Research: Space Physics*,
416 *116*(A10).

- 417 Dhillon, R. S. (2002), Radar studies of natural and artificial waves and instabilities in the
418 auroral ionosphere, Ph.D. thesis, Physics.
- 419 Drell, S., H. Foley, and M. Ruderman (1965), Drag and propulsion of large satellites in
420 the ionosphere: An Alfvén propulsion engine in space, *Journal of Geophysical Research*,
421 *70*(13), 3131–3145.
- 422 Eglitis, P., T. Robinson, M. Rietveld, D. Wright, and G. Bond (1998), The phase speed
423 of artificial field-aligned irregularities observed by CUTLASS during HF modification
424 of the auroral ionosphere, *Journal of Geophysical Research: Space Physics*, *103*(A2),
425 2253–2259.
- 426 Gillies, R., G. Hussey, G. Sofko, K. McWilliams, R. Fiori, P. Ponomarenko, and J.-P. St-
427 Maurice (2009), Improvement of SuperDARN velocity measurements by estimating the
428 index of refraction in the scattering region using interferometry, *Journal of Geophysical
429 Research: Space Physics*, *114*(A7).
- 430 Gillies, R., G. Hussey, G. Sofko, D. Wright, and J. Davies (2010), A comparison of EISCAT
431 and SuperDARN F-region measurements with consideration of the refractive index in
432 the scattering volume, *Journal of Geophysical Research: Space Physics*, *115*(A6).
- 433 Gillies, R., G. Hussey, G. Sofko, P. Ponomarenko, and K. McWilliams (2011), Improve-
434 ment of HF coherent radar line-of-sight velocities by estimating the refractive index in
435 the scattering volume using radar frequency shifting, *Journal of Geophysical Research:
436 Space Physics (1978–2012)*, *116*(A1).
- 437 Gillies, R., G. Hussey, G. Sofko, and K. McWilliams (2012), A statistical analysis of
438 SuperDARN scattering volume electron densities and velocity corrections using a radar
439 frequency shifting technique, *Journal of Geophysical Research: Space Physics*, *117*(A8).

- 440 Greenwald, R., K. Baker, J. Dudeney, M. Pinnock, T. Jones, E. Thomas, J.-P. Villain,
441 J.-C. Cerisier, C. Senior, C. Hanuise, et al. (1995), Darn/SuperDARN, *Space Science*
442 *Reviews*, 71(1-4), 761–796.
- 443 Gurevich, A., K. Zybin, and A. Lukyanov (1995), Stationary striations developed in the
444 ionospheric modification, *Physical review letters*, 75(13), 2622.
- 445 Gurevich, A., H. Carlson, M. Kelley, T. Hagfors, A. Karashtin, and K. Zybin (1999), Non-
446 linear structuring of the ionosphere modified by powerful radio waves at low latitudes,
447 *Physics Letters A*, 251(5), 311–321.
- 448 Gurevich, A., E. Fremouw, J. Secan, and K. Zybin (2002), Large scale structuring of
449 plasma density perturbations in ionospheric modifications, *Physics Letters A*, 301(3),
450 307–314.
- 451 Hooke, W. H. (1968), Ionospheric irregularities produced by internal atmospheric gravity
452 waves, *Journal of Atmospheric and Terrestrial Physics*, 30(5), 795–823.
- 453 Hosokawa, K., K. Shiokawa, Y. Otsuka, T. Ogawa, J.-P. St-Maurice, G. Sofko, and D. An-
454 dre (2009), Relationship between polar cap patches and field-aligned irregularities as
455 observed with an all-sky airglow imager at resolute bay and the PolarDARN radar at
456 Rankin Inlet, *Journal of Geophysical Research: Space Physics*, 114(A3).
- 457 Kelley, M. C., T. L. Arce, J. Salowey, M. Sulzer, W. T. Armstrong, M. Carter, and
458 L. Duncan (1995), Density depletions at the 10-m scale induced by the Arecibo
459 heater, *Journal of Geophysical Research: Space Physics*, 100(A9), 17,367–17,376, doi:
460 10.1029/95JA00063.
- 461 Kosch, M. J., and E. Nielsen (1995), Coherent radar estimates of average high-latitude
462 ionospheric Joule heating, *Journal of Geophysical Research: Space Physics*, 100(A7),

463 12,201–12,215.

464 Kosch, M. J., M. Rietveld, A. Kavanagh, C. Davis, T. Yeoman, F. Honary, and T. Hagfors
465 (2002), High-latitude pump-induced optical emissions for frequencies close to the third
466 electron gyro-harmonic, *Geophysical research letters*, *29*(23).

467 Kosch, M. J., M. Rietveld, A. Senior, I. McCrea, A. Kavanagh, B. Isham, and F. Honary
468 (2004), Novel artificial optical annular structures in the high latitude ionosphere over
469 EISCAT, *Geophysical research letters*, *31*(12).

470 Lehtinen, M. S., and A. Huuskonen (1996), General incoherent scatter analysis and GUI-
471 DAP, *Journal of Atmospheric and Terrestrial Physics*, *58*(1), 435–452.

472 Lester, M., P. Chapman, S. Cowley, S. Crooks, J. Davies, P. Hamadyk, K. McWilliams,
473 S. E. Milan, M. Parsons, D. Payne, et al. (2004), STEREO CUTLASS-a new capability
474 for the SuperDARN HF radars, in *Annales Geophysicae*, vol. 22, pp. 459–473.

475 Leyser, T., B. Thidé, H. Derblom, Å. Hedberg, B. Lundborg, P. Stubbe, and H. Kopka
476 (1990), Dependence of stimulated electromagnetic emission on the ionosphere and pump
477 wave, *Journal of Geophysical Research: Space Physics*, *95*(A10), 17,233–17,244.

478 Moen, J., N. Gulbrandsen, D. Lorentzen, and H. Carlson (2007), On the MLT distribution
479 of F region polar cap patches at night, *Geophysical Research Letters*, *34*(14).

480 Norman, R., M. Parkinson, P. Dyson, et al. (2004), Comparing HF radar backscatter from
481 the southern ocean with ray-tracing results using the IRI model, in *Proceedings of the*
482 *Workshop on the Applications of Radio Science, Hobart, Tasmania*, pp. 18–20.

483 Ponomarenko, P., C. Waters, and F. Menk (2008), Effects of mixed scatter on SuperDARN
484 convection maps, in *Annales Geophysicae*, vol. 26, pp. 1517–1523.

- 485 Pryse, S., K. Dewis, R. Balthazor, H. Middleton, and M. Denton (2005), The dayside
486 high-latitude trough under quiet geomagnetic conditions: Radio tomography and the
487 CTIP model, in *Annales Geophysicae*, vol. 23, pp. 1199–1206.
- 488 Rietveld, M., H. Kohl, H. Kopka, and P. Stubbe (1993), Introduction to ionospheric heat-
489 ing at Tromsø. Experimental overview, *Journal of atmospheric and terrestrial physics*,
490 55(4), 577–599.
- 491 Rietveld, M., M. J. Kosch, N. Blagoveshchenskaya, V. Kornienko, T. Leyser, and T. Yeoman
492 (2003), Ionospheric electron heating, optical emissions, and striations induced by
493 powerful HF radio waves at high latitudes: Aspect angle dependence, *Journal of Geo-
494 physical Research: Space Physics*, 108(A4).
- 495 Rishbeth, H., and A. Van Eyken (1993), EISCAT: Early history and the first ten years of
496 operation, *Journal of Atmospheric and Terrestrial Physics*, 55(4), 525–542.
- 497 Robinson, R., R. Vondrak, K. Miller, T. Dabbs, and D. Hardy (1987), On calculating
498 ionospheric conductances from the flux and energy of precipitating electrons, *Journal
499 of Geophysical Research: Space Physics*, 92(A3), 2565–2569.
- 500 Senior, A., M. T. Rietveld, N. Borisov, M. Kosch, T. Yeoman, and F. Honary (2004),
501 Multi-frequency HF radar measurements of artificial F-region field-aligned irregularities.
- 502 Sojka, J. J., R. W. Schunk, and J. Whalen (1990), The longitude dependence of the dayside
503 F region trough: A detailed model-observation comparison, *Journal of Geophysical
504 Research: Space Physics*, 95(A9), 15,275–15,280.
- 505 Thomas, E., J. Baker, J. Ruohoniemi, L. Clausen, A. Coster, J. Foster, and P. Erick-
506 son (2013), Direct observations of the role of convection electric field in the formation
507 of a polar tongue of ionization from storm enhanced density, *Journal of Geophysical*

- 508 *Research: Space Physics*, 118(3), 1180–1189.
- 509 Weber, E., J. Klobuchar, J. Buchau, H. Carlson, R. Livingston, O. Beaujardiere, M. Mc-
510 Cready, J. Moore, and G. Bishop (1986), Polar cap F layer patches: Structure and
511 dynamics, *Journal of Geophysical Research: Space Physics*, 91(A11), 12,121–12,129.
- 512 Wright, D., J. Davies, T. K. Yeoman, T. Robinson, and H. Shergill (2006), Saturation and
513 hysteresis effects in ionospheric modification experiments observed by the CUTLASS
514 and EISCAT radars, in *Annales Geophysicae*, vol. 24, pp. 543–553.
- 515 Xu, L., A. Koustov, J. Thayer, and M. McCready (2001), SuperDARN convection and
516 Sondrestrom plasma drift, in *Annales Geophysicae*, vol. 19, pp. 749–759.
- 517 Yeoman, T. K., G. Chisham, L. Baddeley, R. Dhillon, T. Karhunen, T. Robinson, A. Se-
518 nior, and D. Wright (2008), Mapping ionospheric backscatter measured by the Super-
519 DARN HF radars - Part 2: Assessing SuperDARN virtual height models.
- 520 Zhang, Q.-H., B.-C. Zhang, M. Lockwood, H.-Q. Hu, J. Moen, J. M. Ruohoniemi, E. G.
521 Thomas, S.-R. Zhang, H.-G. Yang, R.-Y. Liu, et al. (2013), Direct observations of the
522 evolution of polar cap ionization patches, *Science*, 339(6127), 1597–1600.

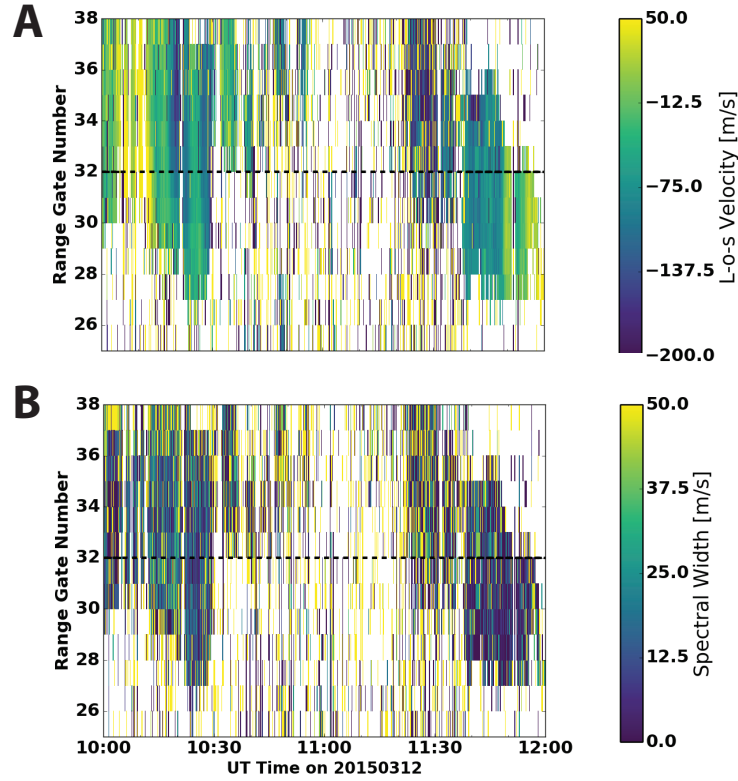


Figure 1. Panel A is the line-of-sight (L-o-s) velocities from the Hankasalmi radar at frequencies of 15 MHz - 18 MHz on March 12, 2015 from 10:00 UT to 12:00 UT at range gates of 25 to 38. The range gates start at 480 km and have 15 km spacing from there. EISCAT is located at approximately range gate 32, where we have placed a black dotted line. Panel B is the spectral widths over the same frequencies and same time period.

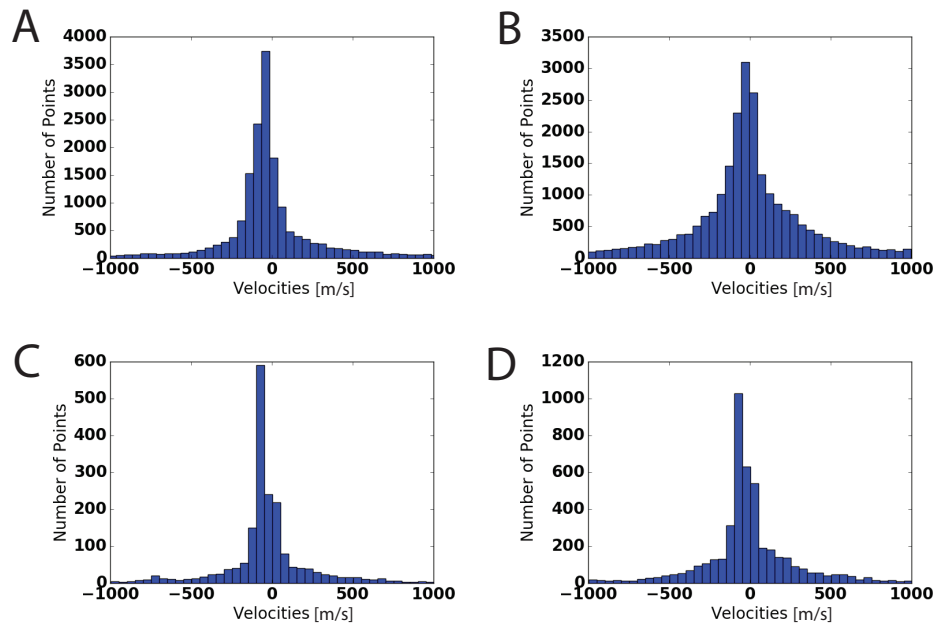


Figure 2. Velocity distributions of each of the major frequency bands from the Hankasalmi radar. Panel A is 15 MHz, B is 16 MHz, C is 17 MHz, and D is 18 MHz for the campaign on March 12, 2015 from 10:00 to 12:00 UT.

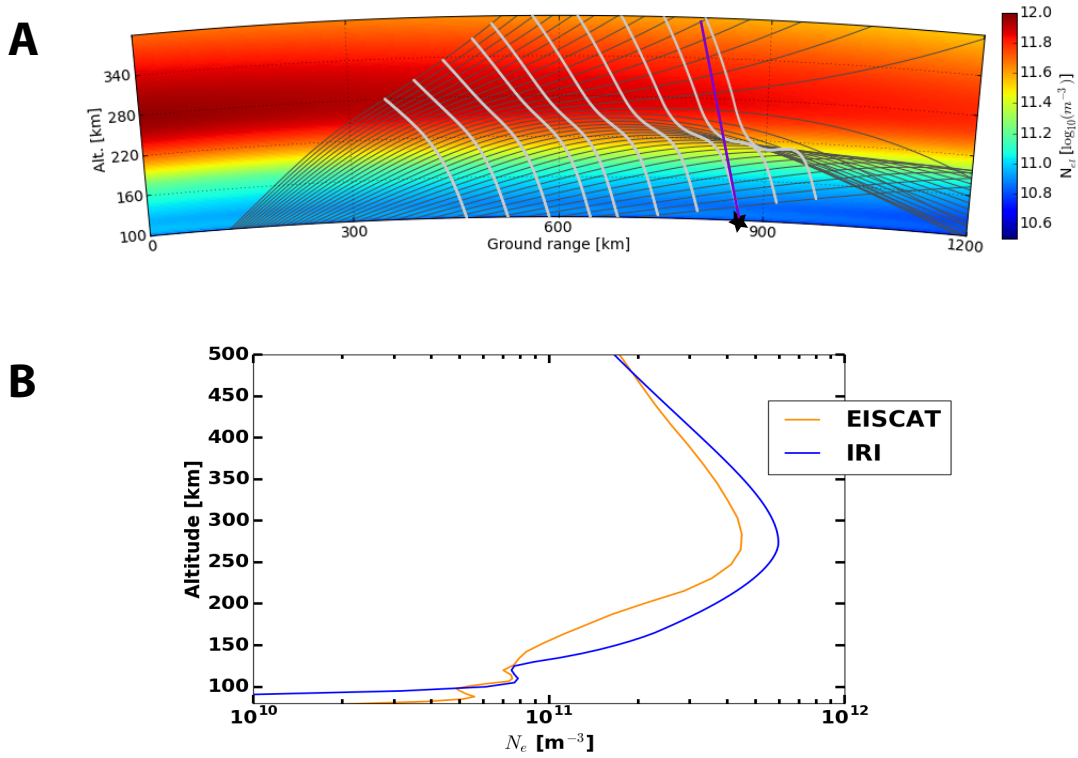


Figure 3. Panel A shows the SuperDARN ray tracing model output for our experiment at 16 MHz for beam 5 on March 12, 2015. The radar-beam elevation angle ranges between 5 and 40 degrees, with 2 degree increments represented by the black lines. The silver lines are every 4th range gate (approximately 60 km) starting at 480 km (range gate 0). The background is N_e from the IRI model. The black star represents the approximate distance to the EISCAT Tromsø site. The purple line represents the magnetic field line at Tromsø, indicating the look direction of the EISCAT Heater. Panel B shows the IRI (blue) and EISCAT (orange) N_e profiles averaged between 10:00 to 12:00 UT on March 12, 2015.

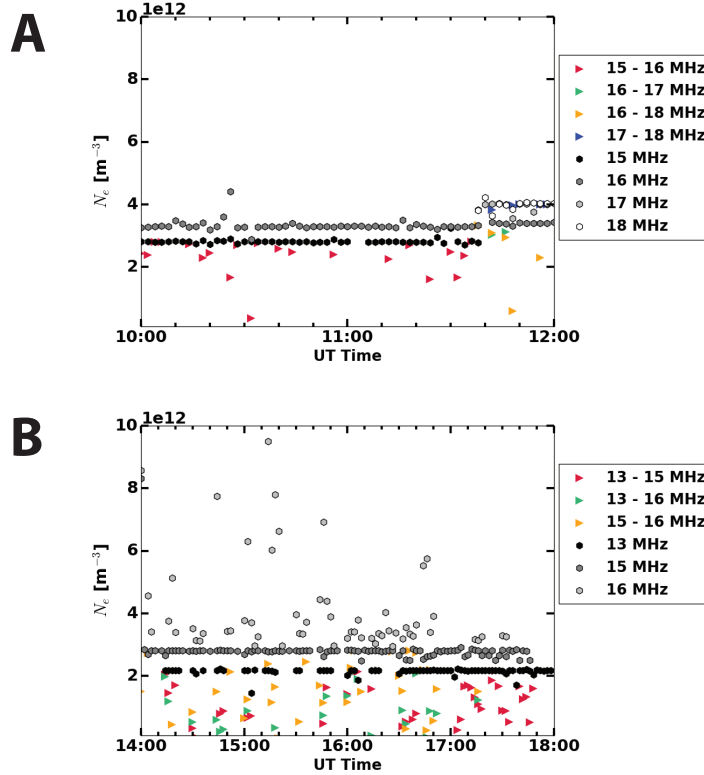


Figure 4. The colored triangles represent the Hankasalmi radar STEREO mode data resampled on a 2 minute cadence for (A) on March 12, 2015 between 10:00 to 12:00 UT. Red is the calculated N_e from the 15 and 16 MHz frequency measurements, green is the 16 and 17 MHz frequency measurements, yellow is the 16 and 18 MHz frequency measurements, and blue is the 16 and 18 MHz measurements. The monochrome hexagons represent the small frequency shift (a few kHz) method of calculating N_e using Hankasalmi data observations over the same time period. The small frequency shifted N_e are also resampled on a 2 minute cadence. Black represents 15 MHz, dark grey is 16 MHz, light grey is 17 MHz, and white is 18 MHz. (B) is similar, with N_e from March 3, 2016 14:00 to 18:00 UT with red as STEREO mode between 13-15 MHz, green between 13 - 16 MHz, and gold between 15 - 16 MHz. The monochrome hexagons represent small frequency shift N_e calculations, with black as 13 MHz, dark grey as 15 MHz, and light grey as 16 MHz. For both methods in Panel A and B, the mean line of sight velocity over range gates 30-35 at each measurement is used in the calculation.

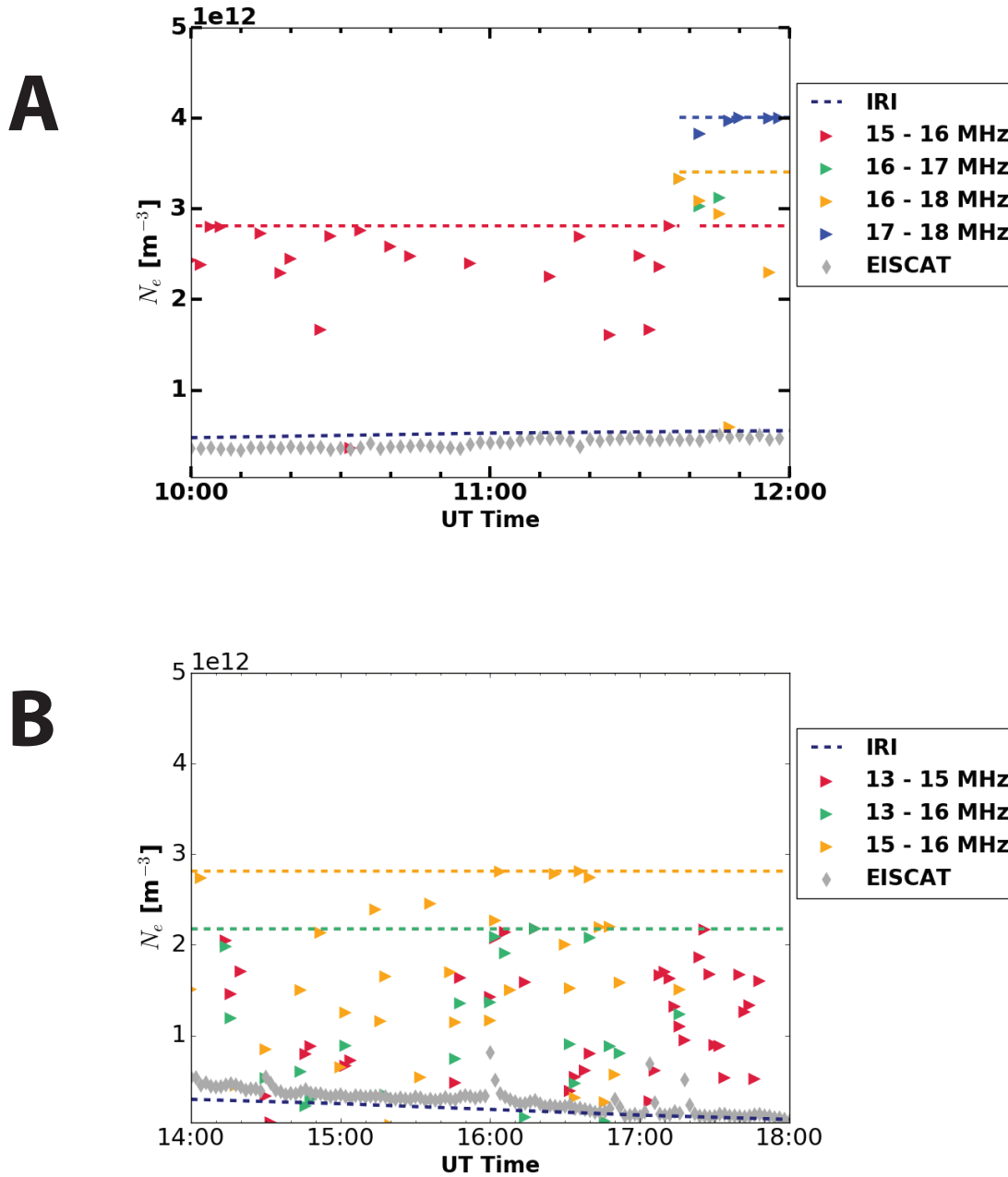


Figure 5. The colored triangles are the calculated N_e from the Hankasalmi STEREO observations for (A) March 12, 2015 from 10:00 to 12:00 UT and (B) March 3, 2016 from 14:00 to 18:00 UT. The shaded diamonds are the EISCAT N_e at 240 km for (A) and 220 km for (B). The navy blue dotted line is IRI N_e at 240 km for (A) and 220 km for (B). The dashed lines are the maximum electron number density possible in regard to plasma frequency. The color of the triangles and dashed lines indicate what frequency pairs were used to calculate N_e .

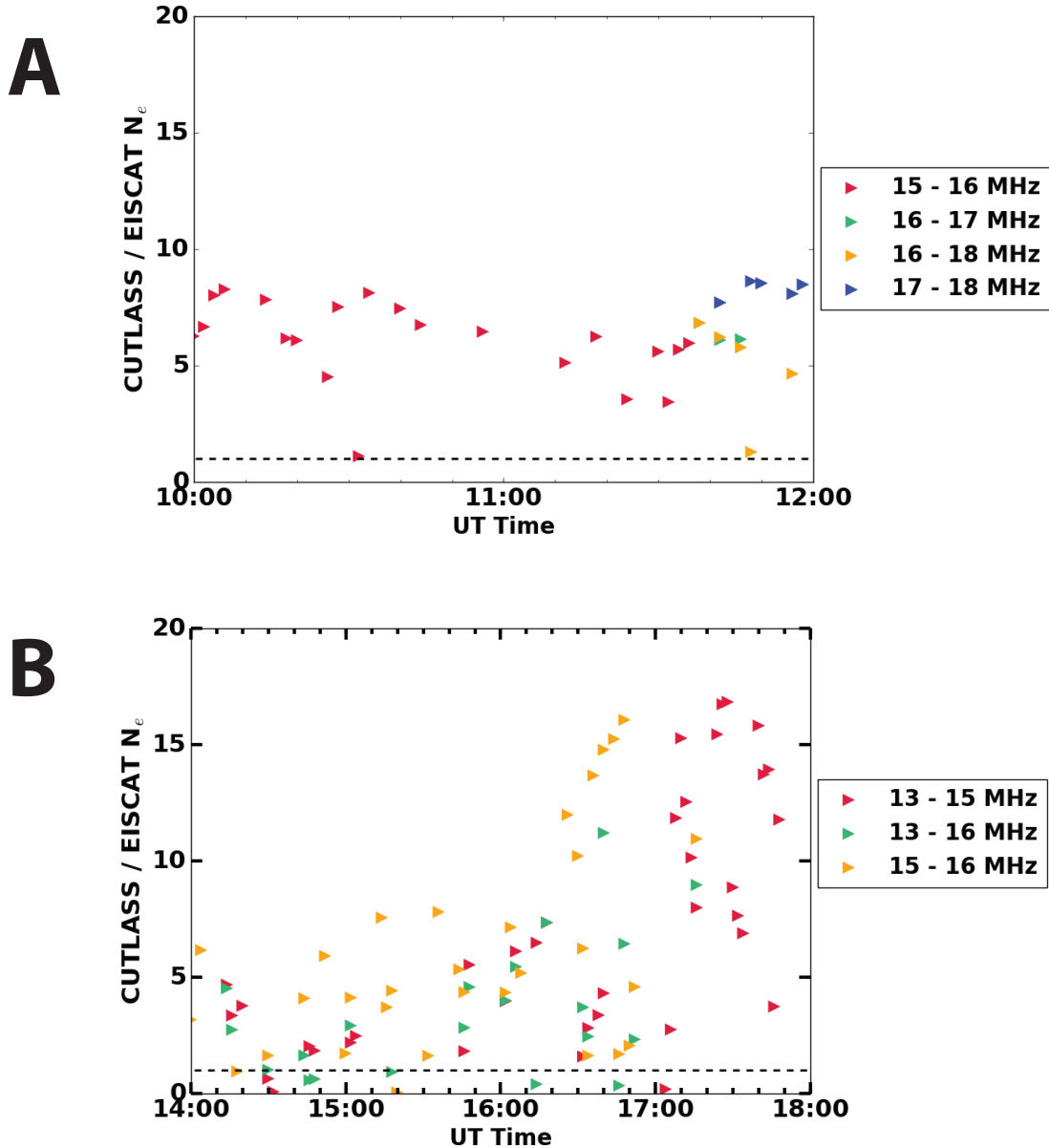


Figure 6. The ratio of N_e calculated from the Hankasalmi and EISCAT radars. The colored triangles are the calculated N_e from the Hankasalmi STEREO method resampled into 2 minute periods for (A) on March 12, 2015 from 10:00 to 12:00 UT and (B) on March 3, 2016 from 14:00 to 18:00 UT and divided by the EISCAT N_e at 240 km for (A) and 220 km for (B) at the same times. The black dotted line is where the Hankasalmi N_e equals the EISCAT N_e . The color of the triangle indicates what frequency pairs were used to calculate N_e . In (A) the green line is under the yellow one and in (B) the red line is under the green one.